Journal of the European Ceramic Society 45 (2025) 117260

Contents lists available at ScienceDirect

Journal of the European Ceramic Society

journal homepage: www.elsevier.com/locate/jeurceramsoc

Novel water-based processing of graphene oxide and sub-micrometric alumina towards tougher and electrically-conductive structural ceramics

Joseph Alemzadeh [a], Rut Benavente [b], Amparo Borrell [b], Carlos Gutiérrez-González [c], Marta Suárez [d], Luis A. Diaz [d], Miguel A. Montes-Morán [e], Clara Blanco [e], Sam L. Evans [a], Victoria G. Rocha [a,e,*]

[a] School of Engineering, Cardiff University, Queen's Buildings, The Parade, Cardiff CF24 3AA, United Kingdom
[b] Instituto de Tecnología de Materiales (ITM), Universidad Politécnica de Valencia (UPV), Camino de Vera s/n, Valencia 46022, Spain
[c] Nanoker Research S.L. Polígono Industrial de Olloniego, parcela 22ª, Nave 5, Oviedo, Asturias 33660, Spain
[d] Centro de Investigación en Nanomateriales y Nanotecnología (CINN-CSIC), Universidad de Oviedo (UO), Principado de Asturias (PA), Avda. de la Vega, 4-6, El Entrego 33940, Spain
[e] Instituto de Ciencia y Tecnologia del Carbono, 33011 Oviedo Spain

ARTICLE INFO

Keywords:
Graphene
Alumina
Ceramic-based composites
Freeze-casting
Spark plasma sintering

ABSTRACT

Balancing the mechanical and functional properties of graphene-reinforced ceramics can be a challenge because agglomeration of the reinforcement must be avoided to minimise microstructural defects and it is difficult to organise the constituents into meaningful structures. The water-based processing strategy that is demonstrated here illustrates the potential to fabricate layered alumina composites using a combination of freeze-casting, vacuum infiltration, and spark plasma sintering. Layers of alumina between 0.5 and 7 μm thick and consist of an average grain size of 0.7 ± 0.4 μm were separated by highly-oriented reduced graphene oxide. Mechanical and functional properties were investigated alongside a monolithic counterpart sintered at 1300 °C. The flexural strength and fracture toughness increased from 262 to 314 MPa and 3.5–5.4 MPa $m^{1/2}$ respectively, whilst electrical conductivity rose by nine orders of magnitude to 10^{-1} S cm^{-1}.

1. Introduction

Since the isolation of graphene in 2004 [1], the 2D hexagonal network of carbon has been studied extensively and incorporated into a multitude of composite materials due to its attractive qualities. Specifically, the development of structural graphene-ceramic composites with a combination of exceptional mechanical and functional properties is an exciting field that is constantly growing. There are a variety of engineering applications in which this class of materials could be useful, including automotive and aerospace components, body armour, energy storage, and structural health monitoring [2–4]. Homogeneous distribution of 2D graphene-related materials (GRMs) such as few-layer graphene (FLG), multilayer graphene (MLG) or graphene oxide (GO) has been attempted within host ceramics such as Al_2O_3, SiC, Si_3N_4, or ZrO_2 to obtain graphene-reinforced composites using traditional mixing of powders along with some other routes involving colloidal processing [5–8]. Electrical conductivity was imparted to these typically insulating ceramics and to some extent an enhancement in mechanical properties was achieved, but issues including agglomeration of the reinforcing phase and induced porosity after sintering can diminish their mechanical functionality [5,9,10]. There has been some success in incorporating graphene into ceramic-based composites, but it has proved difficult to improve both the electrical and mechanical properties. Walker et al. reported a 235 % increase in toughness in Si_3N_4 with only 1.5 vol% of graphene content and observed novel toughening mechanisms [11]. Graphene platelets were wrapped and anchored around individual ceramic grains to resist sheet pullout. However, the hardness of the composite decreased by 42 % and electrical conductivity was not evaluated in this instance. Guo et al. [12]. prepared SiC doped with graphene and found that 5 wt% reinforcement generated composites led to an electrical conductivity of 27.24 S cm^{-1}, but the flexural strength and hardness decreased by 52 % and 42 % respectively – furthermore, the final material was not particularly dense (at 92 % T.D) [12]. Similar performance improvements have been achieved in graphene-Al_2O_3

* Corresponding author at: School of Engineering, Cardiff University, Queen's Buildings, The Parade, Cardiff CF24 3AA, United Kingdom.
E-mail addresses: garciarochav@cardiff.ac.uk, vgarciarocha@incar.csic.es (V.G. Rocha).

https://doi.org/10.1016/j.jeurceramsoc.2025.117260
Received 9 August 2024; Received in revised form 29 January 2025; Accepted 3 February 2025
Available online 4 February 2025

composites. Çelik et al. reported an increase in electrical conductivity of 9 orders of magnitude (to 0.014 S cm^{-1}) after incorporating 9 vol% of graphene, however fracture toughness values were not affected (both in-plane and through thickness) and the hardness fell by 56 % [13]. Shin et al. found that electrical conductivity and fracture toughness rose in rGO-Al_2O_3 composites with increasing rGO content (up to 1 wt%), yet the hardness and elastic modulus dropped slightly [14]. However, this demonstrates the capacity of reaching the percolation threshold for electrical conductivity with a low fraction of GRM. Hence, the trade-off between mechanical and functional properties of graphene-ceramic composites is still a challenge primarily because insufficient attention has been paid to the design of the microstructure.

Processing materials in a way that the microstructure of the material resembles those found in natural materials is an inspirational route to reach elevated mechanical properties [15], which in turn could also help to achieve the electrical conductivity goal. They are usually comprised of a combination of hard (commonly inorganic minerals) and small proportions of soft (biomolecules or polymers) phases with characteristic architectural features from the nanoscale to the macroscale [16]. For example, nacre is comprised of aragonite ($CaCO_3$) tablets with a thickness of approximately 0.5 μm and chitin-based biopolymers (5 wt %) – the tablets themselves are composed of nanograins of the calcium-based mineral, and on the sub-micrometric scale they are arranged in a highly-oriented brick-and-mortar fashion [17]. The result is a lightweight composite with a unique combination of strength and toughness (235–500 MPa and 3.3–9 MPa $m^{1/2}$ respectively, depending on its hydration level and/or testing method). This superior mechanical behaviour compared to its weakly-performing constituents arises due to various extrinsic toughening mechanisms that are generated from the intricacies of its microstructure. An excellent example of a ceramic matrix composite (CMC) inspired by nacre was fabricated by Bouville et al. [18,19]. Layered brick and mortar structures of Al_2O_3, similar in appearance to those present in nacre, were fabricated with a unique combination of high strength (470 MPa), toughness (17 MPa $m^{1/2}$), and stiffness (290 GPa). Their approach combined wet chemistry and advanced processing techniques (freeze casting) with an appropriate selection of materials; Al_2O_3 platelets, Al_2O_3 nanoparticles and glass phase precursors to form an intricate microstructure at different length scales. The global interest in the field of ceramic-based composites – particularly those with arranged microstructures – has expanded over the past 30 years, primarily due to advanced fabrication methods (including additive manufacturing) and rapid consolidation techniques such as Spark Plasma Sintering (SPS) and Field Assisted Sintering Technology (FAST). Recently, Sun et al. produced high performance CMCs by incorporating an ordered graphene array that was formed by microwaving expanded graphite [20]. Graphene networks comprised of FLG were infiltrated with liquid ceramic precursors and sintered by SPS to create highly-oriented FLG-ceramic composites that contained 5 vol% reinforcement. SEM images showed the final layer thickness of the CMCs was no smaller than 2 μm which is quite large compared to the dimensions of nacre's aragonite tablets, however the mechanical and wear properties were outstanding. Moreover, a novel approach to infiltrate a hydrophobic graphene network using an Al_2O_3-based suspension that contains an amphiphilic polymer (Pluronic F127) demonstrated that brick and mortar structures using graphene as a soft phase are feasible [21]. However, in this work the layer thickness was about the size of the porous scaffolds (spanning between 5 and 15 μm) which is an order of magnitude higher than the target dimension of 0.5 μm. Mechanical and functional properties were not evaluated in this investigation.

This work aimed to tackle the challenge of balancing improvements in mechanical and functional properties in graphene-Al_2O_3 composites with nacre-inspired features. In this study, a novel, water-based processing route is presented to fabricate layered rGO-Al_2O_3 composites that possess highly-oriented reinforcement. A freeze-casting step generated ceramic material oriented along one plane, whilst utilisation of a suitable graphene precursor, i.e. GO, circumvented issues with excessive graphene agglomeration during processing. Large porous alumina scaffolds of 30 mm diameter were created using unidirectional freeze-casting, dried and pre-sintered at 900 °C, then subject to vacuum-assisted infiltration with water-based suspensions of GO, and finally consolidated using SPS. The sintering method granted two key benefits: the retention of the architectural features generated during the casting step, and an environment to thermally reduce GO into rGO to re-establish the electrical properties by partly restoring the sp^2-hybridised carbon network. Testing aimed to demonstrate that using low quantities (<1 wt%) of partially reduced GO which is arranged throughout a host ceramic material can improve the fracture properties whilst simultaneously achieving functionality such as electrical conductivity.

2. Experimental

2.1. Materials

Ceramic suspensions were prepared using α-alumina powder (BA15-W white aluminium oxide, d_{50} = 0.1 μm, Baikowski), 10 wt% polyvinyl alcohol solution (>95 %, Thermofisher), sucrose (>99 %, Merck), DOLAPIX CE 64 (Zschimmer and Schwarz) as a dispersant, and graphene oxide (1 wt% dispersion in water, average flake size = <10 μm, Graphenea).

2.2. Preparation of ceramic scaffolds through freeze-casting

0.5 wt% DOLAPIX CE64 wrt. ceramic content was magnetically stirred into water at 600 rpm, then the ceramic powder was added followed by the remaining additives (4 wt% sucrose wrt·H_2O, 1.4 wt% PVA solution wrt. ceramic content). Ultrasonication (UIP1000hdT, 1000 W/20 kHz, Hielscher) was then performed with 70 % power output for 5 min with a 2 minute pause halfway. Cylindrical specimens (30 mm diameter, 35 mm height) were freeze-cast using a set-up described in previous literature with a cooling a rate of 5 °C min^{-1} [21]. Once frozen, materials were placed in a freeze-dryer (Lablyo-85, Frozen in Time) for 72 h. Scaffolds were then pre-sintered in air using a muffle furnace (1700 HTC, Carbolite Gero) up to 900 °C in two stages: up to 120 °C at 2 °C min^{-1} for 1 h, then to 900 °C at 5 °C min^{-1} for 30 min.

2.3. Infiltration of porous alumina with GO suspensions

Water-based suspensions of GO were prepared with a speed-mixer (DAC 800.1 FVZ SpeedMixer, Synergy Devices) operating at 1800 rpm for 5 min. Degassing followed for 10 min using a vacuum chamber (DS-26P vacuum degassing system, Easycomposites). GO suspensions of 0.25 wt% were prepared through dilution and its concentration verified by weighing freeze-dried aliquots. GO suspensions were pipetted over pre-sintered scaffolds and subject to reduced pressure (roughly −1 bar) for 15 min by virtue of the degassing equipment. Infiltrated scaffolds were frozen for 2 h, then freeze-dried for 72 h.

2.4. SPS of alumina-based materials

SPS (HP D 10-SD SPS, FCT Systeme GmbH) was performed on alumina-based materials as powders or composite pre-forms. Graphite moulds and pistons were used for the sintering, covered with soft graphite felt in order to avoid radiation heat loss. Sintering was performed at 1300 °C, with a uniaxial pressure of 50 MPa, heating and cooling rates of 50 °C min^{-1}, and a dwell time of 5 min. A composite was also sintered at 1500 °C to better understand the thermal and electrical properties of alumina-rGO composites.

2.5. Characterisation and material testing

The content of rGO within the sintered composite was assessed in a

thermogravimetric analyser (TGA/SDTA 851e, Mettler Toledo) with air up to 1000 °C at 5 °C min^{-1} after grinding the composite below 63 μm. The theoretical density of the composite was calculated with the rule of mixtures, taking the density of alumina as 3.99 gcm^{-3} and partially reduced GO as 1.9 g cm^{-3} [22,23]. The density of sintered samples was evaluated using Archimedes' principle in water. The particle size distribution of as-received alumina and prepared suspensions was measured with a particle size analyser (Mastersizer 3000, Malvern Panalytical). The lateral size of GO flakes was measured following dilution in water to ~10 ppm and deposition onto Si-SiO_2 (300 nm) substrate. 125 flakes were observed using an optical microscope (DMLM microscope, Leica) and analysed using Fiji software [24]. Diffraction patterns were obtained using XRD (Siemens D5000 diffractometer, Bruker) with Cu (K_α) radiation as the X-ray source. All scans were performed between 2θ values of 5–80° in increments of 0.02 and a scan speed of 1 °min^{-1}. Raman spectra were collected with a confocal Raman microscope (inVia Qontor, Renishaw PLC) with a green laser (532 nm) operating at 25 mW. Spectrum acquisition conditions were 30 s exposure with a 50x ultra-long working distance objective. For each sample, spectra from at least seven different spots were taken. I_D/I_G ratios were calculated from the area of the D (1330 cm^{-1}) and G (1580 cm^{-1}) bands of each spectrum. Average values are given in this work with typical standard deviations below 10 % of those values. FESEM (Crossbeam 1540XB, Carl-Zeiss) of materials (sputtered with Au/Pd when necessary) was taken at 5 kV with corresponding software (SmartSEM® V5.05 XB, Carl-Zeiss). Micrographs were analysed using Fiji to determine the grain size; up to 200 grains were analysed. One alumina scaffold was also assessed using a modified μ-CT scanner (225 kVp Nikon/Xtek HMX system, Nikon Metrology) with 160 kV and a voxel size of 4.52 μm. A smaller section was also evaluated using an X-ray microscope CT scanner (160 kVp Zeiss Xradia Versa 510 system, Carl Zeiss) with 110 kV and a 688 nm voxel size. Post-processing was performed using 3D Slicer (http://www.slicer.org) and Fiji [25].

Hardness was determined using a universal hardness indenter (NOVA 360, InnovaTest) fitted with a Vickers indenter. ASTM E384-17 was followed, indenting specimens polished to a 1 μm finish at 1 kgf for 10 seconds. Fiji was used to measure diagonal lengths after capturing images through optical microscopy. 10 indentations were performed to determine an average. Monolithic alumina fracture toughness was estimated using the Vickers Indentation Fracture (VIF) method with the same hardness equipment. Indentations were made at 30 kgf for 10 seconds and the formula developed by Anstis et al. [26]. was used to calculate fracture toughness. 5 indentations were performed and investigated using SEM. The alumina-0.8rGO composite SPSed at 1300 °C fracture toughness measurement (K_{IC}) using the single-edge-notched-beam (SENB) technique was performed with a universal testing machine (4411, Instron, USA). Seven beams with dimensions 2 × 3.5 × 25 mm were evaluated (a/W= 0.4 and notch radius ≈100 μm), following ASTM C1421 guidelines. Flexural strength was evaluated in 4-point flexure using a universal testing machine (All-roundLine Z050, Zwick-Roell) and following ASTM C1161 guidelines. 4 specimens (approximately 25 × 2 × 2 mm) were tested where sufficient material was tested, and fracture surfaces were investigated using FESEM. Thermal diffusivity was measured between 25 and 750 °C in 100 ml min^{-1} of Ar on square-shaped specimens (10 × 10 × 2 mm) using a laser flash analyser (LFA Microflash apparatus, NETZSCH). Graphite suspension (GRAPHIT 33, Kontakt Chemi) was sprayed onto monolithic alumina as they were white-ivory in colour. The relationship between temperature and specific heat capacity was evaluated with a calorimeter (Calvet C80, Setaram) from 25 to 155 °C (then extrapolated to 750 °C) at a rate of 0.2 °C min^{-1}. Thermal conductivity was then calculated as a result. Electrical resistivity of the composites was assessed using 4-probe resistance measurements on a bar-shaped specimen (approximately 20 × 3.2 × 1.9 mm). Ag paste was applied to the end faces of five specimens and resistance was calculated from reading the voltage through a source measure unit (Fluke 45 Dual Display Multimeter, Fluke, USA) at a span of 14.8 mm whilst applying constant current between 0.01 and 0.50 mA using a potentiostat (VMP-3e, BioLogic, France). Electrical conductivity was calculated as the inverse of the resistivity value.

3. Results and discussion

3.1. Fabrication of layered rGO-alumina composites

The proposed strategy to create a layered graphene-alumina composite is shown in Fig. S1, in which alumina suspensions are freeze-cast and freeze-dried resulting in porous cylindrical scaffolds with channels aligned in parallel with freezing direction (Fig. 1). Labels of freezing direction (FD), pressing direction (PD), and cross section (CS) have been designated to the three planes of freeze-cast materials. The porous materials can be then rotated by 90°, processed further, and consolidated by SPS into disc-shaped specimens whilst preserving the alumina layers perpendicular to the pressing direction. To freeze-cast a large alumina scaffold which possesses thin walls inspired by the length-scale of nacre's features, it was critical to perform high-power ultrasonication on suspensions of spray-dried α-alumina powder (15–150 μm) prior to casting. This enabled the dispersion of as-received agglomerates into

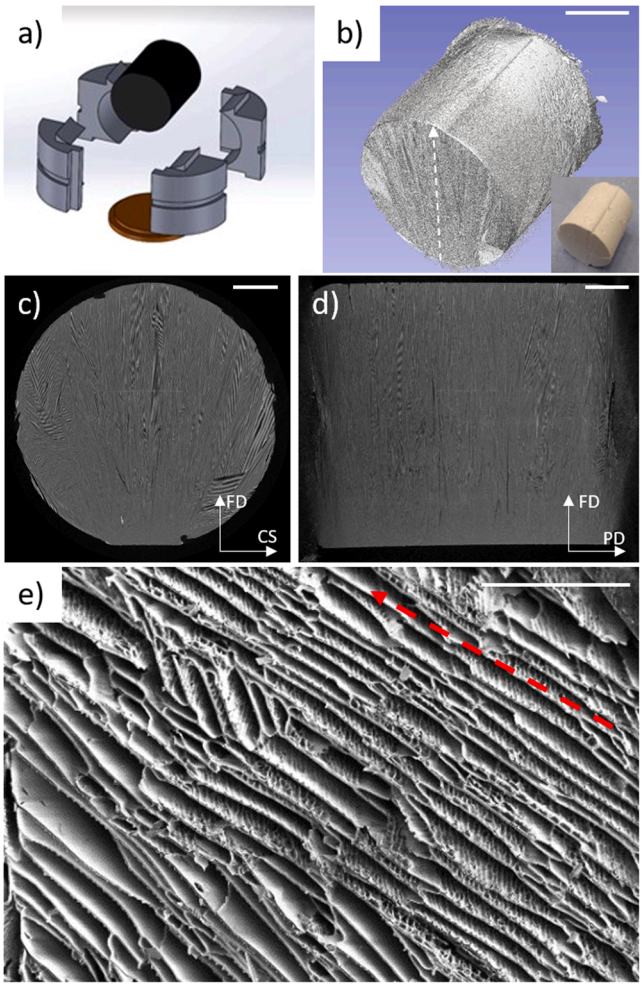

Fig. 1. 30 mm diameter alumina scaffolds fabricated through unidirectional freeze-casting. a) CAD model of 4-piece, PTFE freeze-casting mould fabricated by FDM. b) μ-CT reconstruction of 25 wt% alumina scaffold – scale bar = 10 mm. Inset displays photograph of the specimen. c) and d) μ-CT orthoslices through the FD-CS and FD-PD planes respectively – scale bars = 5 mm. e) SEM of the porous lamellar structure from water-based freeze-casting along the FD-CS plane – scale bar = 500 μm. The red arrow represents the direction of freezing.

finer sub-micrometric grains that are approximately 150 nm in size as shown by SEM (Fig. S2a and S2b) and PSD analysis (Fig. S2c). The particle size distribution vastly decreased to below 0.25 μm after 5 minutes of processing for suspensions with ceramic loadings between 25 and 40 wt% (approximately 7.7–14.4 vol%). The XRD pattern (Fig. S2d) shows the presence of α-phase alumina without any observable peaks arising from other phases.

The combination of high-power ultrasonication and addition of additives (described in Section 2.2) for low-to-moderate solid loading suspensions enabled the successful freeze-casting of sub-micrometric alumina into 30 mm diameter × 35 mm height specimens within a 4-piece PTFE mould (Fig. 1a). Casting in an orientation in which ice grows along the cylindrical diameter allowed the as-obtained alumina green body (inset of Fig. 1b) to be fitted within a 30 mm SPS die set such that the directionally-aligned channels were eventually oriented perpendicular to the direction of pressing. This favours the assembly of a layered composite structure. Labels of freezing direction (FD), pressing direction (PD), and cross section (CS) have been designated to the three planes of freeze-cast materials. Fig. 1c and d provides μ-CT slices through various planes obtained from the computational restoration of a whole alumina scaffold cast from a 25 wt% suspension. The directionality of the porous architecture is easily identifiable, especially with visualisation through the FD-CS plane. The image of the FD-PD plane (Fig. 1d and S3) also shows a lack of porosity within the scaffold in the first couple of millimetres that is close to the freezing surface. The long-range, lamellar appearance of the ceramic walls is a result of using water as a solvent and a controlled freezing rate [27–29]. More extensive examination of the freeze-cast architecture using SEM (Fig. 1e) shows the wall thickness ranged from 0 to 10 μm and the pore size ranged from 15 to 70 μm (40 μm average), which are easily accessible to the GO flakes in a later processing step, which possess an average lateral size of 8 ± 2 μm (Fig. S4a and S4b). Optimisation of the architectural features generated by freeze casting was performed by tuning the solid loading of alumina powder. Fig. S5 shows histograms for 25–40 wt% alumina scaffolds which illustrates that the average wall thickness increases as the solid loading is raised, whilst the pore size shows little change. Suspensions containing 25 wt% solid loading were selected for further processing based on these findings. The green bodies of alumina (inset of Fig. 1b) were quite fragile, thus prior to further processing a pre-sintering step at 900 °C was carried out to simultaneously remove the casting additives and allow for better manipulation.

Fig. 2 shows some steps in the subsequent infiltration process to successfully introduce GO as the reinforcing phase. High uptake of a 0.25 wt% GO suspension within a pre-sintered alumina scaffold (of 25 wt% solid loading) was achieved through vacuum-assisted infiltration after the lower and upper sections of the scaffold were removed: this sectioning was carried out after the pre-sintering step. Fig. 2c shows a partially infiltrated scaffold without removing the mentioned sections and Fig. 2d shows much better results after sectioning. Alumina-GO preforms were then SPSed at 1300 °C, 50 MPa pressure, heating/

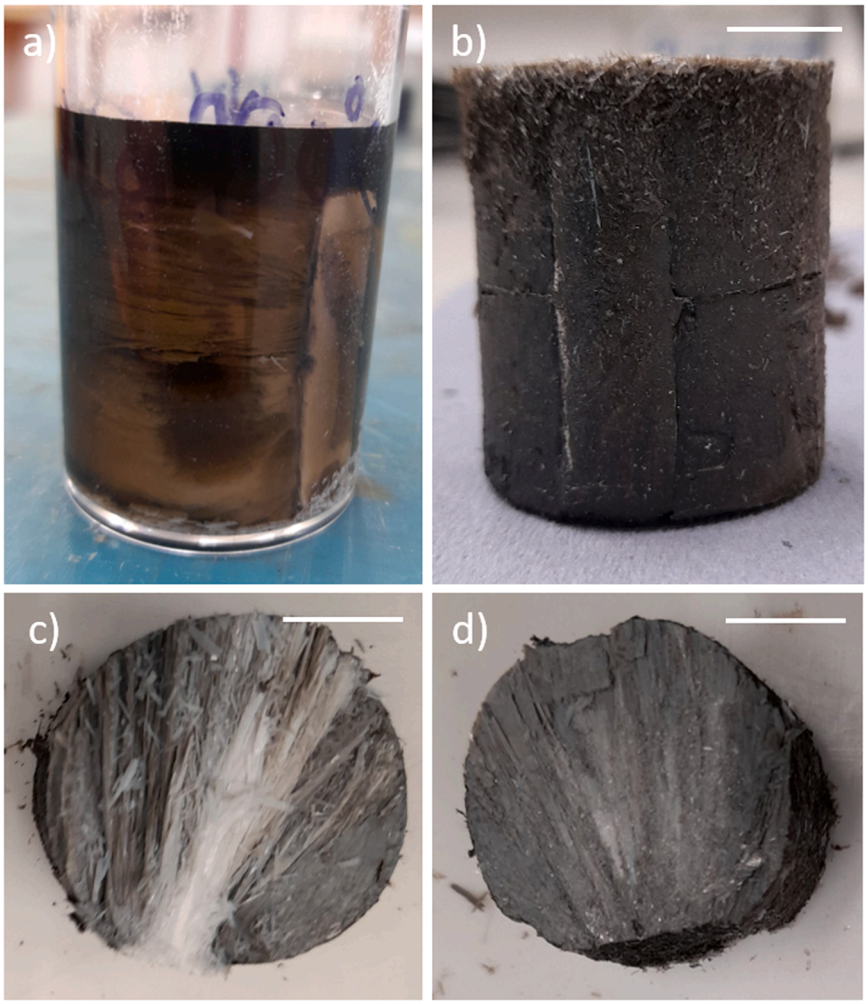

Fig. 2. Photographs illustrating the process of infiltrating freeze-cast alumina scaffolds with 0.25 wt% water-based GO suspensions. a) Alumina scaffold immersed in GO suspension before vacuum-assisted infiltration. b) Alumina-GO pre-form after infiltration, freezing and drying – scale bar = 10 mm. c) Infiltrated scaffold with no physical change and d) After lower and upper sections have been removed – scale bars = 10 mm.

cooling rates of 50 °C min^{-1} and a dwell time of 5 min to generate 30 mm discs with a thickness of roughly 2.2 mm and a mass of 6.5 g. Monolithic alumina was fabricated (from the as-received powder) using the same conditions for comparison. Both materials were considered dense, reaching 99.2 and 99.7 % T.D. respectively. SEM images in Fig. 3 show the microstructure of both materials at different magnifications. While the monolithic alumina had an isotropic microstructure with an average grain size of 1 μm, the composite material clearly exhibits a layered microstructure with highly-oriented layers of reinforcement along the thickness (PD axis) of the specimen. The incorporation of graphene-like reinforcement also led to a refinement in the grain size of the alumina matrix from 1 ± 0.5 to 0.7 ± 0.4 μm. rGO that is generated during SPS lies between alumina layers that are between 0.5 and 7 μm thick (5–15 μm before consolidation). This is still an order of magnitude larger than the ceramic components found in nacre (0.3–0.5 μm depending on the class of mollusc) [17], however the final wall thickness (after SPS) is comparable to other works in the field of bio-inspired, freeze-cast structures [30,31]. The final content of rGO within the host ceramic was found to be 0.8 wt% (1.7 vol%) for the sintered composite (Fig. S6), hence the composite was labelled as "alumina-0.8rGO".

3.2. Mechanical testing of rGO-alumina composites

Considering that monolithic and alumina-0.8rGO fabricated in this study possess similar physical characteristics (i.e., grain size and density) it is interesting to compare their mechanical properties. Table 1 illustrates the results that were obtained for monolithic alumina and alumina-0.8rGO. The composite's microhardness has reduced slightly (roughly 8 %), whilst the flexural strength and the fracture toughness have increased by approximately 20 and 54 % respectively.

Vickers indentations were made across the FD—PD plane to determine the hardness of alumina-based materials. Monolithic alumina reached a hardness of 21.9 GPa whilst after reinforcement with a low proportion (<1 wt%) of rGO this value decreased to 20.2 GPa. This small reduction is indicative of adding a low amount of reinforcement that is more compliant than the ceramic grains that surround it [31,32]. Separate tests were performed across the PD-CS plane to verify if the dispersion of rGO in a different orientation affected the hardness, but no evidence was found to suggest a change in behaviour. Fracture surfaces in Fig. S7 show microstructures of monolithic and rGO-reinforced alumina specimens after 4-point flexure tests in which the flexural strength increased from 262 to 314 MPa. The monolithic alumina

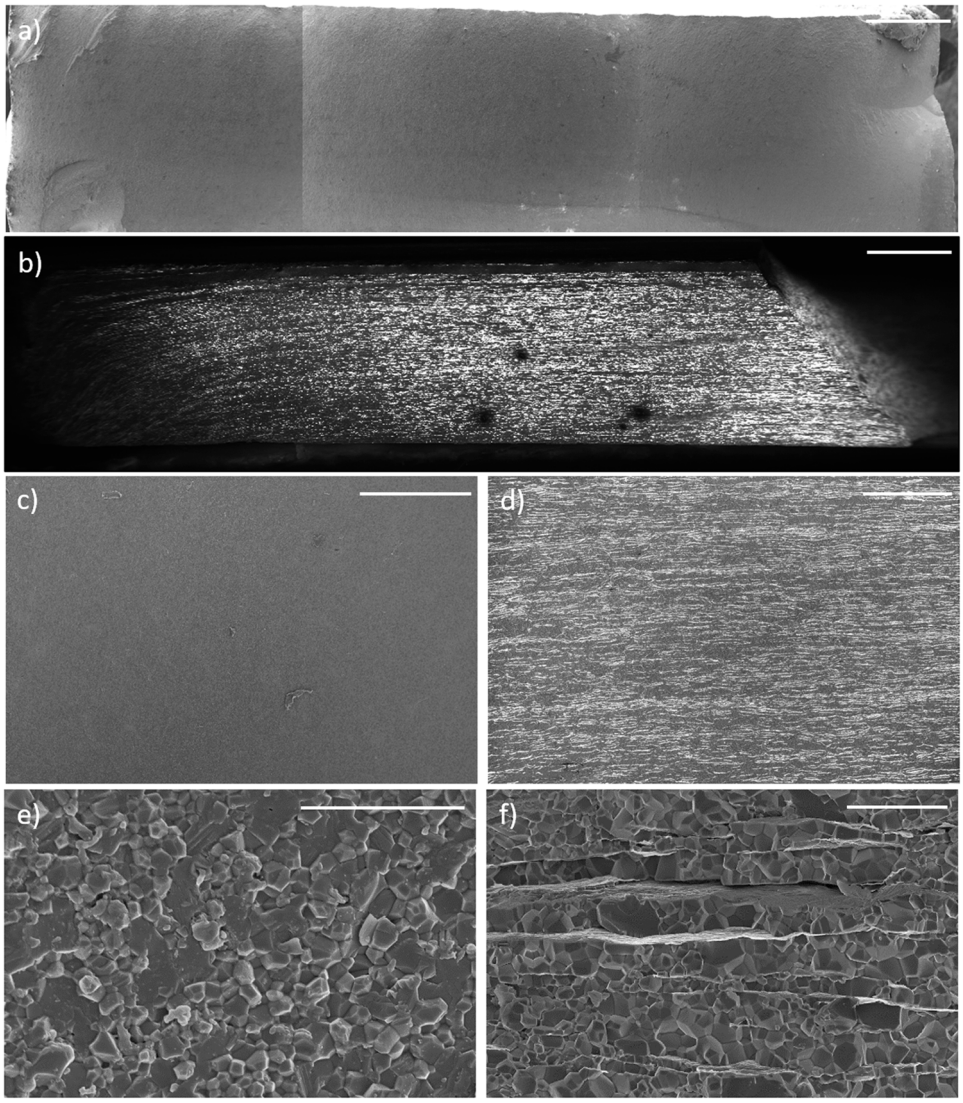

Fig. 3. SEM images of alumina-based materials observed along the FD-PD plane. a) Bulk microstructure of alumina – scale bar = 1 mm. b) Bulk microstructure of composite – scale bar = 1 mm. c) Low magnification image of alumina – scale bar = 200 μm. d) Low magnification image of composite – scale bar = 200 μm. e) High magnification image of alumina – scale bar = 5 μm. f) High magnification image of composite – scale bar = 10 μm.

Table 1
The calculated mechanical properties for alumina and the rGO-reinforced composite.

Material	Density (gcm^{-3})	Theoretical density (%)	Grain size (μm)	Hardness (GPa)	Flexural strength (MPa)	Fracture toughness (MPa $m^{1/2}$)
Alumina	3.96	99.2	1.0 ± 0.5	21.9 ± 0.1	262 ± 35	3.5 ± 0.3 (VIF)
Alumina-0.8rGO	3.93	99.5	0.7 ± 0.4	20.2 ± 0.3	314 ± 32	5.41 ± 0.35 (SENB)

fracture surface appears smooth and homogeneous (Fig. S7a), whilst the surface of alumina-0.8rGO clearly shows a layered microstructure (Fig. S7b) where areas of rGO material appear to have been pulled out from the ceramic matrix (Fig. S7c and S7d). SEM images displayed in Fig. S8 show the indentations made in monolithic and rGO-reinforced alumina at 30 kg. The cracks from the apices of the indentation made in monolithic alumina were quite linear which is representative of brittle failure in ceramic materials. In contrast, due to its highly anisotropic microstructure, the cracking pattern in alumina-0.8rGO showed preferential crack propagation along the FD axis from both the apices and the sides of the indentation. Cracks appear to be slightly shorter (than those in monolithic alumina), whilst several of them have been deflected towards the FD axis. The indentations themselves were slightly larger due to the decrease in microhardness – overall, the fracture toughness increased in the composite from 3.5 to 5.41 MPa $m^{1/2}$.

The increase in fracture toughness by GRM addition into alumina matrices has been widely reported, and while many studies observed a strong dependence on the wt% of filler, the results mostly depend on the degree of GRM agglomeration and composite microstructure, thus for equal wt% GRM, toughness can be found very different [5,13,14,32,33,34]. This is reflected in Fig. 4 where the most relevant studies sintered by SPS and tested by SENB methods have been plotted against the GRM wt%. At low wt% GRM the increase in toughness is between 10 % and 50 %. Close to the wt% of the GRM used in this work, Chen et al. [35] fabricated composites with above 60 % toughness increment with respect to monolithic alumina at higher temperature and not showing a high degree of anisotropy. It can be observed that the alumina-0.8rGO composite SPSed at 1300 °C show a remarkable increment of 54 % in fracture toughness with respect to monolithic alumina which can be mainly attributed to the highly anisotropic layered microstructure achieved by incorporating graphene oxide through the novel water-based processing route presented. The only work with a similar degree of anisotropy that reported a significantly higher toughness is that by Sun et al. [20]. However, in addition to using a much higher GRM loading, the complex processing route chosen comprised to infiltrate organic ceramic precursors in a microwaved expanded graphite

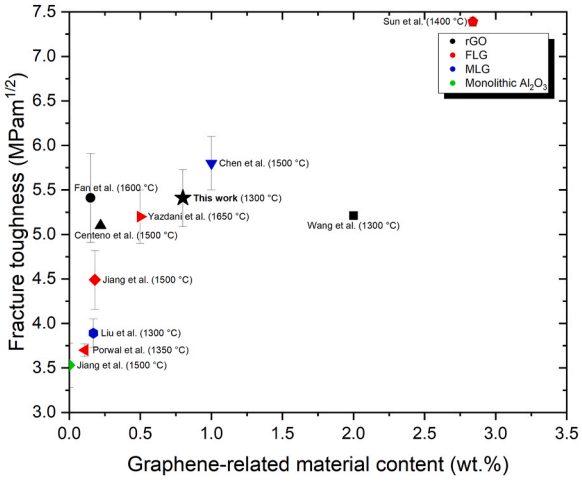

Fig. 4. Plot of SENB fracture toughness values compared to the mass fraction found in the literature for alumina-GRM materials [20,35–42]. Some reports did not provide a standard deviation value but have been included. A value for monolithic alumina (in green) has been provided from Jiang et al. [39].

source while in this work graphene oxide as precursor of graphene is combined with alumina, thus being far simpler.

The improvement in fracture toughness and flexural strength for the alumina-0.8rGO composite can be attributed to extrinsic toughening mechanisms (Fig. 5) that have been induced due to the addition of rGO within the alumina matrix. It was previously illustrated that the deformation patterns from Vickers indentations displayed deflected cracks predominantly along the FD axis. This deflection can be related to the layer-by-layer fashion in which rGO is distributed through the alumina matrix, promoting propagation along the interfaces between the host and reinforcing components (as shown in Fig. 5a). In addition, debonding between the two components can be observed (in Fig. 5b and c) along cracks in several regions that the rGO flakes are located. Crack bridging and branching are also evident in Fig. 5c. It was previously mentioned that the pull-out of both ceramic and highly-oriented rGO components was visible in fracture surfaces after 4-point flexure tests (Fig. 5d), which contributes towards toughening [11,33,34]. The wavy, wrinkled appearance of many of the rGO flakes may also promote an increase in toughness. Flexural strength increased simultaneously, although it did not rise proportionally which does suggest the presence of some defective regions in the composite's microstructure such as multi-layer agglomerates of rGO.

3.3. Electrical/thermal behaviour

Fig. 6 illustrates the measured thermal conductivities along the PD axis for alumina-based materials, including a composite sintered at 1500 °C, showing a clear decrease in the out-of-plane conductivity after reinforcement with rGO which is complemented by Raman data. The decrease in conductivity is lower when sintering at higher temperature, attributed to the greater order of the rGO that was realised. As the processing temperature increased, there was a clear reduction in the intensity of the defect peak (D peak) at 1380 cm^{-1} shown in the calculated the D/G ratios, combined with a narrower FWHM of the G peak at 1580 cm^{-1}. This suggests that the composite sintered at 1500 °C had a highly-ordered graphene-like reinforcement, whilst the composite consolidated at 1300 °C contained graphene-like material which was still moderately disordered. Fig. S9 provides a comparison of the Raman spectra of the composite materials to that of the initial GO. The reduction of the GO within both composite materials is evidenced by the D' shoulder occurring at ca. 1620 cm^{-1} [43,44]. Also, the Raman signal in the second order region (>1800 cm^{-1}) is already noticeable in the sample sintered at 1300 °C, which also constitutes a proof of GO reduction. Increasing the sintering temperature up to 1500 °C improved the order of the rGO by reducing the defects of the graphene lattice, most likely by increasing the rGO layer size and/or by reducing the rGO in-plane defects. Still, the formation of rGO in the alumina composites prepared here is far from that of graphite.

Previous work has demonstrated a similar decreasing trend in thermal conductivity when reinforcing ceramics with a graphene-based filler [14,45,46]. Previous theoretical and experimental work focused on understanding the effects of microstructural factors during heat conduction and found that materials with larger grain sizes and fewer grain boundaries possess a lower interfacial thermal resistance (Kapitza resistance) due to fewer phonon scattering events [47–50]. It is thought that because the composite's microstructure is more refined, the higher number of grain boundaries increases phonon scattering – this is regardless of the 2D-reinforcement that has been incorporated. Although, it is thought that this would compete with the degree of rGO

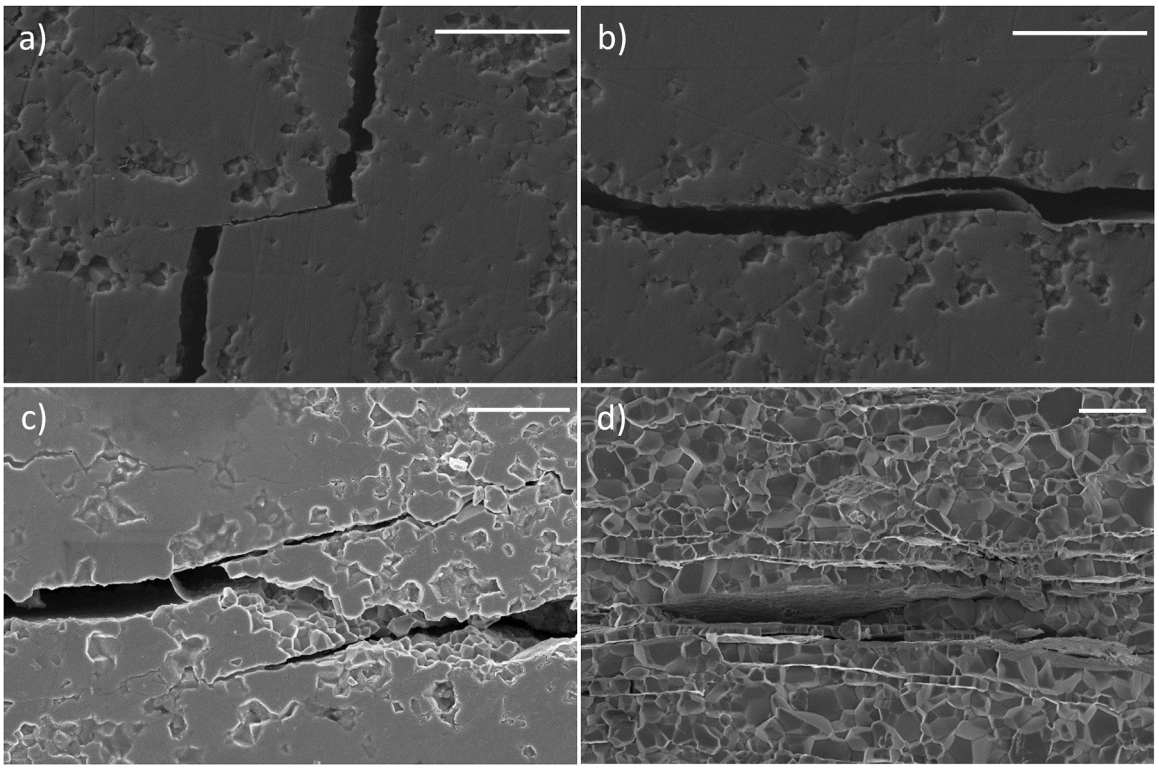

Fig. 5. SEM images of alumina-0.8rGO demonstrating a variety of toughening mechanisms. a) crack deflection, b) crack bridging and rGO debonding, c) crack branching and intragranular fracture, d) pull-out of matrix and reinforcement – scale bars = 5 μm. Higher contrast thresholds were set for c) and d) so that exposed grains were in view.

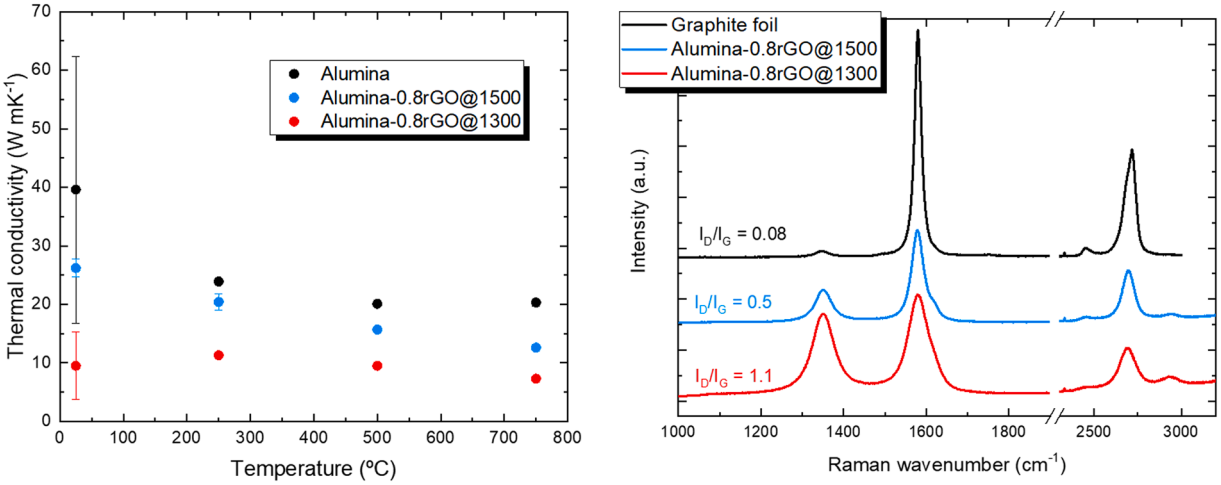

Fig. 6. Thermal conductivity measurements and Raman spectra for alumina and alumina-rGO composites. Raman data for graphite foil was also collected for reference.

reduction in changing the thermal transport properties for rGO-reinforced alumina, because the grain sizes for materials sintered at 1300 °C and 1500 °C were 0.7 ± 0.4 μm and 0.9 ± 0.5 μm respectively. Fig. S10 shows SEM images of the two composites which illustrates a slight difference in their grain sizes. However, this can only be reflective of the materials' thermal conductivity measured in the PD axis. Considering that the microstructure of the fabricated composites is anisotropic, we further suggest that the thermal conductivity measured along the FD axis will alter from the result obtained along the PD axis.

As the previous Raman data demonstrated a reduction in GO after SPS, the electrical behaviour of the primary composites sintered at 1300 °C and 1500 °C was evaluated. Table 2 shows the in-plane electrical

Table 2
Calculated in-plane electrical properties of alumina-based materials measured along the FD axis. Values for alumina are provided from the literature [5].

Material	Electrical resistivity (Ω cm)	Electrical conductivity (S cm^{-1})
Alumina @1300 °C	1×10^{9}	1×10^{-9}
Alumina-0.8rGO @1300 °C	1.73 (± 0.25)	0.58
Alumina-0.8rGO @1500 °C	5.51×10^{-1} (± 0.18)	1.81

resistivities (and conductivities) of alumina and composite samples. As an electrically insulating material, alumina exhibits a very high resistance and therefore possesses very limited conductivity. However, after the addition of highly oriented rGO there was a stark difference in the composite material by at least nine orders of magnitude (Table 2). Bearing in mind that electro-discharge machining can be applied to machine ceramic-based materials if electrical resistivity is below 100 Ω cm, the obtained results at low fractions of carbon are significant. It is therefore assumed that the percolation threshold has been reached in the specimen with the low mass fraction of rGO that has been incorporated.

Regarding other studies on alumina GRM materials, conductivity values differ significantly as evidenced in Fig. 7. For example, nacre-inspired composites investigated by Liang et al. [51] demonstrated an electrical conductivity over ten times higher (6.3 S cm^{-1}) than the core section of our specimens. The microstructure of their nacre-like material was comparable to the one produced here, containing layer upon layer of alternating alumina and graphene-like components. However, they state that they used a chemical reduction step (with hydrazine hydrate) to partially deoxygenate GO, which was intentionally avoided in this work. Moreover, they did not provide any details on the fraction of reinforcement that was incorporated within the host matrix or the sintering temperature using in hot pressing. This makes it difficult to relate the reported high conductivity to any microstructural component except for the highly-oriented stacking of rGO. Work by Shin et al. [14] on rGO-alumina showed a lower conductivity whilst introducing a similar amount of filler material (1 wt%, compared to 0.8 wt%) [14]. The conductivity was determined to be 7×10^{-3} S cm^{-1} which is much lower than the alumina-0.8rGO composites. In agreement with the alumina-0.8rGO composites´Raman characterisation (Fig. 6) a three-fold conductivity value was achieved by increasing the sintering temperature by 200 °C. Therefore, it is worth mentioning that the electrical conductivity obtained by Ivanov et al. [52] is quite high considering the low sintering temperature, however the filler was integrated through chemical vapor deposition.

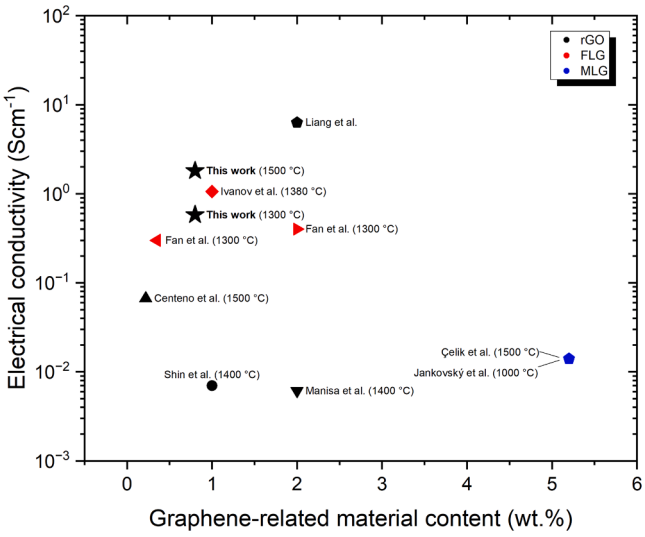

Fig. 7. Plot of electrical conductivities compared to the mass fraction found in the literature for alumina-GRM materials [5,7,13,14,53,54–56,52].

4. Conclusions

In summary a novel, water-based processing route has been developed to fabricate alumina-graphene materials inspired by nacre that possess higher flexure strength and superior toughness and electrical conductivity when compared to their monolithic counterpart. Microstructural analysis revealed consistent and highly-oriented layering of graphene-like reinforcement throughout host alumina which introduced several extrinsic toughening mechanisms including crack deflection, crack bridging, and pull-out. The electrical percolation threshold was reached using this fabrication strategy of infiltrating a 3D ceramic matrix with a 2D graphene precursor, and a significant electrical conductivity was achieved at 1500 °C which is due to sufficient reduction of GO to rGO. This work offers a new route to creating layered composite materials and we suggest that this water-based strategy can be extended to ceramic-metal and ceramic-ceramic composites to create multifunctional materials provided that the compatibility of materials (such as hydrophilicity, shrinkage and thermal expansion, sintering temperatures) is considered.

CRediT authorship contribution statement

Carlos Gutierrez-González: Methodology, Writing – review & editing. **Marta Suárez:** Data curation, Methodology, Validation, Writing – review & editing. **Rut Benavente:** Writing – review & editing, Funding acquisition. **Luis A. Díaz:** Data curation, Methodology, Validation. **Amparo Borrell:** Writing – review & editing, Funding acquisition. **Miguel A. Montes-Morán:** Writing – review & editing, Writing – original draft, Validation, Methodology, Investigation. **Clara Blanco:** Writing – review & editing, Validation, Funding acquisition. **Sam L. Evans:** Writing – review & editing, Writing – original draft, Supervision, Project administration, Methodology, Investigation, Funding acquisition, Formal analysis, Conceptualization. **Victoria G. Rocha:** Writing – review & editing, Validation, Supervision, Project administration, Methodology, Investigation, Funding acquisition, Formal analysis, Conceptualization. **Joseph Alemzadeh:** Writing – review & editing, Writing – original draft, Methodology, Investigation, Data curation, Conceptualization.

Declaration of Competing Interest

The authors declare that they have no known competing financial interests or personal relationships that could have appeared to influence the work reported in this paper.

Acknowledgements

The authors would like to thank the financial support provided by the Engineering and Physical Sciences Research Council through the EPSRC grant EP/N509449/1, and Cardiff University. μ-CT work was supported by the National Research Facility for Lab X-ray CT (NXCT) through the EPSRC grant EP/T02593X/1. J. Alemzadeh would like to thank Prof. G. Min for laboratory access within Cardiff University. V.G. Rocha would like to thank the Spanish Government (Ramon y Cajal fellowship, RYC2018-024404-I) and the support from the Principado de Asturias (FICYT)-European Union (FEDER) (Project PCTI-Asturias IDI/2021/ 000015) R. Benavente would like to thank the financial support provided by the Generalitat Valenciana through the grant CIGE/2021/076. For the purpose of open access, the author has applied a CC BY public copyright licence to any Author Accepted Manuscript version arising.

Appendix A. Supporting information

Supplementary data associated with this article can be found in the online version at doi:10.1016/j.jeurceramsoc.2025.117260.

References

[1] K.S. Novoselov, A.K. Geim, S.V. Morozov, D. Jiang, Y. Zhang, S.V. Dubonos, I. V. Grigorieva, A.A. Firsov, Electric field effect in atomically thin carbon films, Science 306 (1979) (2004) 666–669, https://doi.org/10.1126/science.1102896.

[2] K. Markandan, J.K. Chin, M.T.T. Tan, Recent progress in graphene based ceramic composites: a review, J. Mater. Res. 32 (2017) 84–106, https://doi.org/10.1557/jmr.2016.390.

[3] C. Ramírez, M. Belmonte, P. Miranzo, M.I. Osendi, Applications of ceramic/graphene composites and hybrids, Materials 14 (2021) 2071, https://doi.org/10.3390/ma14082071.

[4] C. Ramírez, 10 years of research on toughness enhancement of structural ceramics by graphene, Philos. Trans. R. Soc. A: Math. Phys. Eng. Sci. 380 (2022), https://doi.org/10.1098/rsta.2022.0006.

[5] A. Centeno, V.G. Rocha, B. Alonso, A. Fernández, C.F. Gutierrez-Gonzalez, R. Torrecillas, A. Zurutuza, Graphene for tough and electroconductive alumina ceramics, J. Eur. Ceram. Soc. 33 (2013) 3201–3210, https://doi.org/10.1016/j.jeurceramsoc.2013.07.007.

[6] X. He, L. Feng, Z. Zhang, X. Hou, X. Ye, Q. Song, Y. Yang, G. Suo, L. Zhang, Q.-G. Fu, H. Li, High-performance multifunctional carbon–silicon carbide composites with strengthened reduced graphene oxide, ACS Nano 15 (2021) 2880–2892, https://doi.org/10.1021/acsnano.0c08924.

[7] A. Weibel, A. Flaureau, A. Pham, G. Chevallier, J. Esvan, C. Estournès, C. Laurent, One-step synthesis of few-layered-graphene/alumina powders for strong and tough composites with high electrical conductivity, J. Eur. Ceram. Soc. 40 (2020) 5779–5789, https://doi.org/10.1016/j.jeurceramsoc.2020.06.029.

[8] N.W. Solís, P. Peretyagin, R. Torrecillas, A. Fernández, J.L. Menéndez, C. Mallada, L.A. Díaz, J.S. Moya, Electrically conductor black zirconia ceramic by SPS using graphene oxide, J. Electroceram. 38 (2017) 119–124, https://doi.org/10.1007/s10832-017-0076-z.

[9] C. Ramirez, M.I. Osendi, P. Miranzo, M. Belmonte, F. Figueiredo, A. Castro-Beltrán, M. Terrones, Graphene nanoribbon ceramic composites, Carbon N.Y. 90 (2015) 207–214, https://doi.org/10.1016/j.carbon.2015.04.014.

[10] P. Kun, O. Tapasztó, F. Wéber, C. Balázsi, Determination of structural and mechanical properties of multilayer graphene added silicon nitride-based composites, Ceram. Int. 38 (2012) 211–216, https://doi.org/10.1016/j.ceramint.2011.06.051.

[11] L.S. Walker, V.R. Marotto, M.A. Rafiee, N. Koratkar, E.L. Corral, Toughening in graphene ceramic composites, ACS Nano 5 (2011) 3182–3190, https://doi.org/10.1021/nn200319d.

[12] X. Guo, R. Wang, P. Zheng, Z. Lu, H. Yang, Pressureless sintering of multilayer graphene reinforced silicon carbide ceramics for mechanical seals, Adv. Appl. Ceram. 118 (2019) 409–417, https://doi.org/10.1080/17436753.2019.1634942.

[13] Y. Çelik, A. Çelik, E. Flahaut, E. Suvaci, Anisotropic mechanical and functional properties of graphene-based alumina matrix nanocomposites, J. Eur. Ceram. Soc. 36 (2016) 2075–2086, https://doi.org/10.1016/j.jeurceramsoc.2016.02.032.

[14] J.-H. Shin, J. Choi, M. Kim, S.-H. Hong, Comparative study on carbon nanotube- and reduced graphene oxide-reinforced alumina ceramic composites, Ceram. Int. 44 (2018) 8350–8357, https://doi.org/10.1016/j.ceramint.2018.02.024.

[15] U.G.K. Wegst, M.F. Ashby, The mechanical efficiency of natural materials, Philos. Mag. 84 (2004) 2167–2186, https://doi.org/10.1080/14786430410001680935.

[16] R.O. Ritchie, The conflicts between strength and toughness, Nat. Mater. 10 (2011) 817–822, https://doi.org/10.1038/nmat3115.

[17] J. Sun, B. Bhushan, Hierarchical structure and mechanical properties of nacre: a review, RSC Adv. 2 (2012) 7617–7632, https://doi.org/10.1039/c2ra20218b.

[18] F. Bouville, E. Maire, S. Meille, B. Van De Moortèle, A.J. Stevenson, S. Deville, Strong, tough and stiff bioinspired ceramics from brittle constituents, Nat. Mater. 13 (2014) 508–514, https://doi.org/10.1038/nmat3915.

[19] F. Bouville, E. Maire, S. Meille, B. Van De Moortèle, A.J. Stevenson, S. Deville, Correction: Corrigendum: strong, tough and stiff bioinspired ceramics from brittle constituents, Nat. Mater. 16 (2017) 1271, https://doi.org/10.1038/nmat4982.

[20] C. Sun, Y. Huang, Qiang Shen, W. Wang, W. Pan, P. Zong, L. Yang, Y. Xing, C. Wan, Embedding two-dimensional graphene array in ceramic matrix, Sci. Adv. 6 (2020), https://doi.org/10.1126/sciadv.abb1338.

[21] G. Menendez, T. Kynaston, I.J. Villar-Garcia, M. Gao, S.L. Evans, V.G. Rocha, Enabling water-based processing of graphene/alumina composites using an infiltration approach with amphiphilic triblock copolymers, J. Eur. Ceram. Soc. 42 (2022) 6574–6582, https://doi.org/10.1016/j.jeurceramsoc.2022.07.009.

[22] L.G. Guex, B. Sacchi, K.F. Peuvot, R.L. Andersson, A.M. Pourrahimi, V. Ström, S. Farris, R.T. Olsson, Experimental review: chemical reduction of graphene oxide (GO) to reduced graphene oxide (rGO) by aqueous chemistry, Nanoscale 9 (2017) 9562–9571, https://doi.org/10.1039/C7NR02943H.

[23] L. Torrisi, M. Cutroneo, A. Torrisi, L. Silipigni, Measurements on five characterizing properties of graphene oxide and reduced graphene oxide foils, Phys. Status Solidi A Appl. Mater. Sci. 219 (2022) 2100628, https://doi.org/10.1002/pssa.202100628.

[24] J. Schindelin, I. Arganda-Carreras, E. Frise, V. Kaynig, M. Longair, T. Pietzsch, S. Preibisch, C. Rueden, S. Saalfeld, B. Schmid, J.-Y. Tinevez, D.J. White, V. Hartenstein, K. Eliceiri, P. Tomancak, A. Cardona, Fiji: an open-source platform for biological-image analysis, Nat. Methods 9 (2012) 676–682, https://doi.org/10.1038/nmeth.2019.

[25] A. Fedorov, R. Beichel, J. Kalpathy-Cramer, J. Finet, J.-C. Fillion-Robin, S. Pujol, C. Bauer, D. Jennings, F. Fennessy, M. Sonka, J. Buatti, S. Aylward, J.V. Miller, S. Pieper, R. Kikinis, 3D Slicer as an image computing platform for the Quantitative Imaging Network, Magn. Reson Imaging 30 (2012) 1323–1341, https://doi.org/10.1016/j.mri.2012.05.001.

[26] G.R. Anstis, P. Chantikul, B.R. Lawn, D.B. Marshall, A critical evaluation of indentation techniques for measuring fracture toughness: I, Direct crack measurements, J. Am. Ceram. Soc. 64 (1981) 533–538, https://doi.org/10.1111/j.1151-2916.1981.tb10320.x.

[27] H. Schoof, J. Apel, I. Heschel, G. Rau, Control of pore structure and size in freeze-dried collagen sponges, J. Biomed. Mater. Res. 58 (2001) 352–357, https://doi.org/10.1002/jbm.1028.

[28] S. Deville, E. Saiz, A.P. Tomsia, Ice-templated porous alumina structures, Acta Mater. 55 (2007) 1965–1974, https://doi.org/10.1016/j.actamat.2006.11.003.

[29] S. Deville, Freeze-casting of porous ceramics: a review of current achievements and issues, Adv. Eng. Mater. 10 (2008) 155–169, https://doi.org/10.1002/adem.200700270.

[30] S. Deville, E. Saiz, R.K. Nalla, A.P. Tomsia, Freezing as a path to build complex composites, Science 311 (1979) (2006) 515–518, https://doi.org/10.1126/science.1120937.

[31] U.G.K. Wegst, H. Bai, E. Saiz, A.P. Tomsia, R.O. Ritchie, Bioinspired structural materials, Nat. Mater. 14 (2015) 23–36, https://doi.org/10.1038/nmat4089.

[32] J. Liu, H. Yan, K. Jiang, Mechanical properties of graphene platelet-reinforced alumina ceramic composites, Ceram. Int. 39 (2013) 6215–6221, https://doi.org/10.1016/j.ceramint.2013.01.041.

[33] H. Porwal, P. Tatarko, S. Grasso, J. Khaliq, I. Dlouhý, M.J. Reece, Graphene reinforced alumina nano-composites, Carbon N.Y. 64 (2013) 359–369, https://doi.org/10.1016/j.carbon.2013.07.086.

[34] L. Wang, J. Bi, W. Wang, Y. Chen, R. Liu, X. Sun, Microstructure and mechanical properties of nacre-like alumina toughened by graphene oxide, Ceram. Int. 45 (2019) 8081–8086, https://doi.org/10.1016/j.ceramint.2019.01.013.

[35] Y.-F. Chen, J.-Q. Bi, C.-L. Yin, G.-L. You, Microstructure and fracture toughness of graphene nanosheets/alumina composites, Ceram. Int. 40 (9) (2014) 13883–13889, https://doi.org/10.1016/j.ceramint.2014.05.107.

[36] H. Porwal, P. Tatarko, S. Grasso, J. Khaliq, I. Dlouhý, M.J. Reece, Graphene reinforced alumina nano-composites, Carbon 64 (2013) 359–369, https://doi.org/10.1016/j.carbon.2013.07.086.

[37] A. Centeno, V.G. Rocha, B. Alonso, A. Fernández, C.F. Gutierrez-Gonzalez, R. Torrecillas, A. Zurutuza, Graphene for tough and electroconductive alumina ceramics, J. Eur. Ceram. Soc. 33 (15–16) (2013) 3201–3210, https://doi.org/10.1016/j.jeurceramsoc.2013.07.007.

[38] B. Yazdani, H. Porwal, Y. Xia, H. Yan, M.J. Reece, Y. Zhu, Role of synthesis method on microstructure and mechanical properties of graphene/carbon nanotube toughened Al2O3 nanocomposites, Ceram. Int. 41 (8) (2015) 9813–9822, https://doi.org/10.1016/j.ceramint.2015.04.054.

[39] X. Liu, Y. Fan, J. Li, L. Wang, W. Jiang, Preparation and mechanical properties of graphene nanosheet reinforced alumina composites, Adv. Eng. Mater. 17 (1) (2015) 28–35, https://doi.org/10.1002/adem.201400231.

[40] J. Liu, H. Yan, K. Jiang, Mechanical properties of graphene platelet-reinforced alumina ceramic composites, Ceram. Int. 39 (6) (2013) 6215–6221, https://doi.org/10.1016/j.ceramint.2013.01.041.

[41] X. Fan, N. Ni, X. Wang, W. Hao, F. Guo, X. Zhao, Mechanically isotropic alumina prepared by spark plasma sintering: the role of pyrolytic carbon and multilayer graphene, J. Eur. Ceram. Soc. 41 (7) (2021) 4242–4251, https://doi.org/10.1016/j.jeurceramsoc.2021.01.056.

[42] K. Wang, Y. Wang, Z. Fan, J. Yan, T. Wei, Preparation of graphene nanosheet/alumina composites by spark plasma sintering, Mater. Res. Bull. 46 (2) (2011) 315–318, https://doi.org/10.1016/j.materresbull.2010.11.005.

[43] A.A.K. King, B.R. Davies, N. Noorbehesht, P. Newman, T.L. Church, A.T. Harris, J. M. Razal, A.I. Minett, A new raman metric for the characterisation of graphene oxide and its derivatives, Sci. Rep. 6 (2016) 19491, https://doi.org/10.1038/srep19491.

[44] X. Díez-Betriu, S. Álvarez-García, C. Botas, P. Álvarez, J. Sánchez-Marcos, C. Prieto, R. Menéndez, A. de Andrés, Raman spectroscopy for the study of reduction mechanisms and optimization of conductivity in graphene oxide thin films, J. Mater. Chem. C Mater. 1 (2013) 6905, https://doi.org/10.1039/c3tc31124d.

[45] R. Sedlák, A. Kovalčíková, V. Girman, E. Múdra, P. Rutkowski, A. Dubiel, J. Dusza, Fracture characteristics of SiC/graphene platelet composites, J. Eur. Ceram. Soc. 37 (2017) 4307–4314, https://doi.org/10.1016/j.jeurceramsoc.2017.04.067.

[46] P. Rutkowski, P. Klimczyk, L. Jaworska, L. Stobierski, A. Dubiel, Thermal properties of pressure sintered alumina-graphene composites, J. Therm. Anal. Calor. 122 (2015) 105–114, https://doi.org/10.1007/s10973-015-4694-x.

[47] K. Watari, K. Hirao, M. Toriyama, K. Ishizaki, Effect of grain size on the thermal conductivity of Si3N4, J. Am. Ceram. Soc. 82 (2004) 777–779, https://doi.org/10.1111/j.1151-2916.1999.tb01835.x.

[48] Z. Wang, J.E. Alaniz, W. Jang, J.E. Garay, C. Dames, Thermal conductivity of nanocrystalline silicon: importance of grain size and frequency-dependent mean free paths, Nano Lett. 11 (2011) 2206–2213, https://doi.org/10.1021/nl1045395.

[49] H. Dong, B. Wen, R. Melnik, Relative importance of grain boundaries and size effects in thermal conductivity of nanocrystalline materials, Sci. Rep. 4 (2014) 7037, https://doi.org/10.1038/srep07037.

[50] D.S. Smith, F. Puech, B. Nait-Ali, A. Alzina, S. Honda, Grain boundary thermal resistance and finite grain size effects for heat conduction through porous polycrystalline alumina, Int. J. Heat Mass Transf. 121 (2018) 1273–1280, https://doi.org/10.1016/j.ijheatmasstransfer.2018.01.082.

[51] L. Liang, C. Huang, C. Wang, X. Sun, M. Yang, S. Wang, Y. Cheng, Y. Ning, J. Li, W. Yin, Y. Li, Ultratough conductive graphene/alumina nanocomposites, Compos. Part A Appl. Sci. Manuf. 156 (2022) 106871, https://doi.org/10.1016/j.compositesa.2022.106871.

[52] R. Ivanov, I. Hussainova, M. Aghayan, M. Drozdova, D. Pérez-Coll, M.A. Rodríguez, F. Rubio-Marcos, Graphene-encapsulated aluminium oxide nanofibers as a novel type of nanofillers for electroconductive ceramics, J. Eur. Ceram. Soc. 35 (2015) 4017–4021, https://doi.org/10.1016/j.jeurceramsoc.2015.06.011.

[53] Y. Fan, L. Wang, J. Li, J. Li, S. Sun, F. Chen, L. Chen, W. Jiang, Preparation and electrical properties of graphene nanosheet/Al2O3 composites, Carbon N.Y. 48 (2010) 1743–1749, https://doi.org/10.1016/j.carbon.2010.01.017.
[54] Y. Fan, W. Jiang, A. Kawasaki, Highly conductive few-layer graphene/Al2O3 nanocomposites with tunable charge carrier type, Adv. Funct. Mater. 22 (2012) 3882–3889, https://doi.org/10.1002/adfm.201200632.
[55] V.K. Manisa, M. Porter, M.J. Whiting, R.A. Dorey, Effect of processing on the stability and electrical properties of pressureless sintered graphene oxide–alumina composites, Ceram. Int. 48 (2022) 15839–15847, https://doi.org/10.1016/j.ceramint.2022.02.122.
[56] O. Jankovský, P. Šimek, D. Sedmidubský, Š. Huber, M. Pumera, Z. Sofer, Towards highly electrically conductive and thermally insulating graphene nanocomposites: Al2O3-graphene, RSC Adv. 4 (2014) 7418–7424, https://doi.org/10.1039/c3ra45069d.